

1 **Imaging the Kanto Basin bedrock with noise and**
2 **earthquake autocorrelations**

3 **Loïc Viens¹, Chengxin Jiang², and Marine A. Denolle³**

4 ¹Disaster Prevention Research Institute, Kyoto University, Uji, Japan

5 ²Research School of Earth Sciences, The Australian National University, Canberra, ACT, Australia

6 ³Department of Earth and Planetary Sciences, Harvard University, Cambridge, MA, USA

7 **Key Points:**

- 8 • Noise and earthquake autocorrelation functions from a dense seismic network are
9 used to map the bedrock depth of the Kanto Basin, Japan
10 • Both methods recover similar P-wave reflections from the basin bedrock
11 • Our study is the first urban-basin-scale mapping of a complex seismic basement
12 using passive data from a dense seismic network

Corresponding author: Loïc Viens, viens.loic.58r@st.kyoto-u.ac.jp

Abstract

Sedimentary basins can strongly amplify seismic waves from earthquakes. To better predict strong ground motions, thorough knowledge of sediment thickness and internal basin structure is required. This study maps the deep and complex bedrock shape of the Kanto Basin, Japan, using ambient seismic noise and earthquake autocorrelation functions (ACFs). Noise ACFs are computed using one month of continuous data recorded by the vertical component of 287 MeSO-net stations located in the greater Tokyo area. Earthquake ACFs are obtained from the P-wave records at the MeSO-net stations of 50 M_w 6+ teleseismic earthquakes. Both noise and earthquake ACFs exhibit great similarity in P-wave reflections, confirming that the same wavefield is extracted with both methods. We finally map the basin bedrock geometry and find that it is comparable with that from an existing 3-D velocity model.

Plain Language Summary

Sedimentary basins, which lie beneath numerous urban areas, can significantly increase seismic hazard by amplifying incoming seismic waves from earthquakes. This study focuses on the deep and complex Kanto Basin, Japan, which is well known to amplify long-period ground motions that are a potential threat to the numerous urban infrastructures of the greater Tokyo area. We combine measurements from ambient seismic noise and earthquake records at seismic stations of a dense network to derive a map of the sedimentary basin bedrock. We find that both methods yield similar results, which had not been reported before, and that they can be used to infer the geometry of the complex Kanto Basin.

1 Introduction

Sedimentary basins have the potential to strongly amplify and extend the duration of seismic waves from earthquakes, which can pose a threat to urban infrastructures (Anderson et al., 1986; Koketsu & Kikuchi, 2000; Koketsu et al., 2005). The Kanto Basin, Japan, is a large-scale sedimentary structure that underlies the highly populated greater Tokyo area. The basin has a sediment-to-bedrock interface that is locally deeper than 4 km (Figure 1a) and is well known to amplify long-period seismic waves (e.g., Denolle et al., 2014; Furumura & Hayakawa, 2007; Kudo, 1978, 1980; Mamula et al., 1984; Viens et al., 2016). During the last decade, several velocity models have been constructed from various geological and geophysical datasets and have revealed the complex bedrock shape and the internal structure of the basin (Fujiwara et al., 2012; Koketsu et al., 2012; Yamada & Yamanaka, 2012). Among these models, the Japan Integrated Velocity Structure Model (JIVSM, Koketsu et al., 2008, 2012) divides the basin into three layers with P- and S-wave velocities increasing with depth. While the JIVSM is a recent and well used velocity model, seismic wave simulations showed that the model cannot fully explain the long-period ground motions from earthquakes (Takemura et al., 2015; Yoshimoto & Takemura, 2014).

Active seismic surveys are generally used to obtain high-resolution images of the Earth's shallow subsurface, but are expensive and rather impractical in urban areas (Morrice et al., 2001). During the past two decades, passive seismic methods have become very popular to map shallow structures using dense seismic networks. For example, the receiver function (Langston, 1979; Leahy et al., 2012; Liu et al., 2018) and horizontal-to-vertical (H/V) spectral ratio (Guéguen et al., 2007; Nakamura, 1989) methods have been used to obtain detailed images of sedimentary basins. However, both techniques require 3-component seismometers, which are not yet fully standard for temporary station deployments.

Autocorrelation functions (ACFs) of vertical seismic noise records can be used to retrieve the P-wave reflectivity response of the underlying medium, from which the geometry of the structure can then be inferred. The theoretical framework of the method was first introduced by Claerbout (1968) for acoustic waves in 1-D media and later extended to 3-D media (Wapenaar, 2003). Noise ACFs are particularly powerful to image interfaces with strong seismic impedance contrasts, such as sedimentary basin bedrocks (Clayton, 2020; Romero & Schimmel, 2018; Saygin et al., 2017), the Mohorovičić (Moho) discontinuity (Clayton, 2020; Gorbатов et al., 2013; Oren & Nowack, 2016; Tibuleac & von Seggern, 2012), and subducting slabs (Ito et al., 2012).

ACFs can also be computed using P-waves (and their coda) from teleseismic events (e.g., Pham & Tkalčić, 2017). This method takes advantage of the near vertical incidence of teleseismic P-waves beneath seismometers to retrieve the P-wave reflectivity response of the underlying medium. Earthquake ACFs have been used to image shallow structures such as ice sheets (Pham & Tkalčić, 2017; Pham & Tkalčić, 2018), the crust structure (Delph et al., 2019; Tork Qashqai et al., 2019), and the Moho discontinuity (Delph et al., 2019; Pham & Tkalčić, 2017; Tork Qashqai et al., 2019), as well as deep structures such as the Earth's inner core (Huang et al., 2015; Wang et al., 2015).

One major difference between the noise and earthquake ACF methods resides in the nature of the wavefield that is correlated (Tkalčić et al., 2020). While P-waves and their coda from teleseismic earthquakes arrive with an almost vertical incidence angle beneath seismic stations, the seismic noise is mainly generated at the Earth's surface by the coupling of oceans with the solid Earth at long periods (> 1 s) and human activities at short periods (< 1 s). This results in a noise wavefield that is generally dominated by surface waves and that only contains weak body wave energy (Bonney-Claudet et al., 2006; Clayton, 2020). Practically, the different nature of the wavefield affects the convergence of the ACFs. Days-to-weeks of continuous records can be necessary to retrieve a clear P-wave reflectivity response using noise ACFs, whereas the P-wave ACFs from only a few teleseismic events can yield an accurate response of the medium (e.g., Lin & Tsai, 2013, for a station-to-station

correlation setting). Physically, the different nature of the signals that are autocorrelated challenges the interpretation of the extracted seismic wavefield.

To our best knowledge, the literature currently lacks a comparison of the P-wave reflectivity response obtained by both ambient noise and earthquake P-wave coda ACFs. This study fills this gap by taking advantage of a dense seismic network to map the complex Kanto Basin bedrock with both methods. We show that despite having different waveform shapes, both noise and earthquake ACFs can be used to image the bedrock depth. We finally compare our results with the JIVSM and discuss the different features obtained with both the noise and earthquake ACFs.

2 Data and Methods

2.1 Noise ACFs

We use 30 days of data recorded by 287 accelerometers of the Metropolitan Seismic Observation network (MeSO-net, Kasahara et al., 2009; Sakai & Hirata, 2009) from January 1 to 15 and July 1 to 15, 2019. The sensors are buried in 20-m deep boreholes and shown in Figure 1a. The data are first band-pass filtered between 0.05 and 5 Hz (4-pole 2-pass Butterworth bandpass filters are used for all filtering operations), corrected for their instrument response, down-sampled from 200 Hz to 20 Hz, and split into 20-min time series. Each 20-min acceleration waveform is then zero-padded to four times its original length and noise ACFs are calculated in the frequency domain (ω) as

$$\text{ACF}_{Z,Z}(t) = F^{-1}(\hat{a}_Z(\omega)\hat{a}_Z^*(\omega)), \quad (1)$$

where \hat{a} is the Fourier transform of a vertical (Z) zero-padded 20-min acceleration record. The $*$ symbol is the complex conjugate and F^{-1} is the inverse Fourier transform applied to retrieve ACFs in the time domain (represented by t). For each station, the stacking of noise ACFs is performed after rejecting 20-min ACFs with potentially overwhelming amplitudes that would dominate the stack. To do so, we compute a metric as the sum of the mean and the standard deviation of all the 20-min ACF absolute peak amplitudes. Then, we only stack the 20-min ACFs with absolute peak amplitudes smaller than the metric using the phase-weighted stack (PWS, Schimmel & Paulssen, 1997) method (power: 2 and smoothing: 0.1 s). Finally, we band-pass filter the stacked ACFs between 1 and 10 s and only consider the causal part of the ACFs given their strict symmetry. To demonstrate that seasonality has little influence on the noise ACF stability, we show a comparison of the noise ACFs computed either from the data recorded in January or from July in Supplementary Material Figure S1.

To remove the effect of the source function (e.g., zero-time lag spike) and enhance the contribution of the reflectivity response of the medium, we follow the procedure introduced by Clayton (2020). For each station, we subtract the noise ACF with a linear average of all ACFs within a 25-km radius of the site. The 25-km radius is chosen empirically as a trade off between spatial resolution and number of ACFs to average (i.e., number of surrounding stations). We exclude stations/sites with fewer than 10 ACFs to average within that radius to ensure the stability of the average trace. An example of the average trace removal process is shown in Supplementary Material Figure S2. Finally, the noise ACFs are normalized by their absolute peak amplitude.

2.2 Earthquake ACFs

To compute earthquake ACFs, we select 244 M_w 6+ earthquakes which occurred between May 2017 and April 2020 within 30 and 95 degrees of angular distance from the Kanto Basin using the USGS (National Earthquake Information Center, NEIC) catalog (Figure 1b). For each earthquake, we download 120 s-long vertical waveforms at the MeSO-net stations with a 20 Hz sampling rate, starting 20 s before the predicted direct P-wave

132 arrival calculated using the AK135 model (Kennett et al., 1995). We then select earthquakes
 133 with signal-to-noise ratio (SNR) values averaged over the 287 MeSO-net stations larger than
 134 2.5. The SNR is defined as the ratio of the peak absolute amplitude within a 6 s window
 135 after the direct P-wave divided by the root-mean-square of a 15 s noise window starting 20
 136 s before the direct P-wave. Finally, we remove a few of the selected events with no clear
 137 P-wave onsets after visual inspection. The final selection contains the 50 events shown in
 138 Figure 1b.

139 To compute ACFs from P-waves and their coda, we follow the procedure described in
 140 Pham and Tkalčić (2017). For each earthquake, we correct the data for their instrument
 141 response, select a 45 s-long window starting 15 s before the P-wave arrival, and remove
 142 both the mean and trend of the data. Similarly to noise ACFs, earthquake ACFs are
 143 computed in the frequency domain after zero-padding the data to four times their initial
 144 duration. The only difference is that the earthquake spectra are pre-whitened after being
 145 Fourier transformed to mitigate biases towards low frequencies that dominate the earthquake
 146 spectra (Pham & Tkalčić, 2017). Data pre-whitening is performed using the running-mean
 147 average algorithm of Bensen et al. (2007) with a sliding-spectral window of 30 samples
 148 (i.e., 0.67 Hz). The length of the sliding-spectral window does not considerably impact the
 149 time-domain ACFs (Supplementary Material Figure S3). After applying the inverse Fourier
 150 transform, the time-domain ACFs are tapered with a 10-sample (i.e., 0.5 s) Tukey window
 151 to suppress the zero-time-lag spikes and are band-pass filtered between 1 and 10 s. Finally,
 152 the PWS algorithm (power: 2 and smoothing: 0.1 s) is applied to stack the ACFs from the
 153 50 earthquakes. Similarly to noise ACFs, only the causal part is analyzed and the waveforms
 154 are normalized by their absolute peak amplitudes. Note that the average trace removal step
 155 is not performed for the earthquake ACFs.

156 3 Results and discussion

157 We show the noise and earthquake ACFs along Lines 1 to 4 (locations in Figure 1a)
 158 together with the corresponding JIVSM velocity profiles in Figures 2 and 3. For each station,
 159 we first use the JIVSM to compute three theoretical arrival times of P-waves traveling
 160 between the surface and the bedrock interface (Figure 2b). The 2p arrival time corresponds
 161 to a P-wave traveling from the station down to the bedrock interface and back up to the
 162 station. The $2p^2$ and $2p^3$ arrival times are twice and three times the down-then-up path
 163 and therefore have their arrival times being twice and three times that of 2p, respectively.

164 Along the four lines, noise ACFs show clear negative phases near the theoretical 2p
 165 and $2p^3$ arrival times and positive phases near the $2p^2$ arrivals (e.g., Figures 2b, 2f, 3b, and
 166 3f). The polarity changes for the $2p^2$ and $2p^3$ phases are caused by free-surface reflections.
 167 Earthquake ACFs primarily exhibit consistent negative phases near the theoretical 2p arrival
 168 time (Figures 2c, 2g, 3c, and 3g). Moreover, clear positive phases near the theoretical $2p^2$
 169 arrival time can also be observed at some stations along Lines 1–3 (Figures 2c, 2g, and 3c).
 170 The stations that exhibit strong multiples for both noise and earthquake ACFs are generally
 171 located in the area where the four lines intersect.

172 In the following, we focus on the negative phases near the theoretical $2p^3$ and 2p arrival
 173 times for the noise and earthquake ACFs, respectively. For the noise ACFs, the phases near
 174 the theoretical $2p^3$ arrival time are more stable than that near the 2p and $2p^2$ arrival times.
 175 This can be explained by the fact that the 2p and $2p^2$ arrival times are closer to the zero
 176 time lag and therefore more likely to be affected by the average trace removal process and/or
 177 by potential weak reflections from the three internal layers of the basin. To measure the
 178 travel time of the $2p^3$ phase from noise ACFs, we simply select the negative peak values
 179 between the theoretical $2p^3$ arrival time ± 2.5 s. If several negative peaks are found within
 180 the empirically chosen 5-s window, we select the negative peak that is the closest to the
 181 theoretical $2p^3$ arrival time. Note that we also visually inspect the waveforms to manually
 182 adjust a few values (list of manually adjusted stations in Supplementary Material Table S1).

183 The selected travel times are finally divided by three to retrieve the P-wave two-way travel
 184 times shown in Figures 2d, 2h, 3d, and 3h. For the earthquake ACFs, we select the negative
 185 peaks within the theoretical $2p \pm 0.65$ s. For both methods, no value is assigned if
 186 there is no negative peak within the considered time windows (e.g., Figure 3b at 58 km).

187 Along Lines 1 and 2, the bedrock depth varies relatively smoothly along the lines and
 188 we obtain P-wave two-way travel time values from both the noise and earthquake ACFs that
 189 are consistent with the theoretical $2p$ arrival times (Figures 2d and 2h). Along Line 3, which
 190 crosses the western basin edge, the bedrock depth changes more rapidly (Figure 3a). This
 191 leads to slightly more complex noise and earthquake ACFs, especially near the deepest part
 192 of the basin along the line. Nevertheless, the measured P-wave two-way travel time values
 193 from both methods agree well with that predicted from the JIVSM. Along Line 4, which has
 194 its southern end close to the Sagami Trough, noise and earthquake ACFs are also relatively
 195 complex (Figures 3f and 3g). For the first 20 km along Line 4, the bedrock depth from
 196 the JIVSM rapidly increases from 1.5 km to 3 km (Figure 3e). While the measured P-wave
 197 two-way travel times from the noise and earthquake ACFs seem to agree with that from
 198 the JIVSM, the autocorrelograms in Figures 3f and 3g do not exhibit clear phases of such
 199 depth variations. Between 20 and 50 km from the south-western end of Line 4, there is a
 200 rather large discrepancy between the two types of ACFs, with clear negative phases near the
 201 theoretical $2p$ arrival time for the earthquake ACFs compared to the weak amplitude of the
 202 noise ACFs near the theoretical $2p^3$ arrival time. Moreover, the measured P-wave two-way
 203 travel times computed from earthquake ACFs are shorter than that from the noise ACFs
 204 and the JIVSM for this part of Line 4 (Figure 3h). We show in Supplementary Material
 205 Figure S4 that slightly earlier negative peaks could also be chosen for the noise ACFs, which
 206 would yield P-wave two-way travel times consistent with that measured from earthquake
 207 ACFs.

208 For each MeSO-net station, we migrate the P-wave two-way travel time values to depth
 209 using a constant P-wave velocity of 2.53 km/s. This value corresponds to the JIVSM
 210 surface-to-bedrock P-wave velocity averaged over the 287 station locations and is relatively
 211 constant within the basin with a one standard deviation to the mean of 0.1 km/s. We show
 212 the JIVSM, noise ACF, and earthquake ACF bedrock depths in Figures 4a, 4b, and 4c,
 213 respectively. Note that 11 and 17 stations are not displayed in Figures 4b and 4c as no
 214 negative peak was found within the theoretical $2p^3 \pm 2.5$ s and $2p \pm 0.65$ s time windows,
 215 respectively. Both methods show consistent bedrock depths with the JIVSM, with a shallow
 216 bedrock beneath the eastern part of the basin and the mountainous region to the west.
 217 The deepest part of the basin is also well retrieved by both the noise and earthquake ACF
 218 methods. To quantify the depth differences between the models, we finally compute residuals
 219 as the JIVSM bedrock depth minus that from the noise and earthquake ACFs and show
 220 them in Figures 4d and 4e, respectively. The mean of the residuals over all the MeSO-net
 221 stations (μ) is less than 100 m for both methods and the one standard deviations to the
 222 mean (σ) are 290 m and 327 m for the noise and earthquake ACFs, respectively. This
 223 confirms that both noise and earthquake ACFs can be used to map the complex shape of
 224 the Kanto Basin bedrock.

225 The major difference between Figures 4d and 4e is the shallower bedrock area in the
 226 Tokyo/Yokohama region obtained with earthquake ACFs (e.g., cluster of red circles in Figure
 227 4e). As mentioned above, this region corresponds to the area along Line 4 where earlier
 228 negative peaks could also be picked for noise ACFs. This would lead to consistent P-wave
 229 two-way travel times for both methods and a bedrock depth that is up to 1.3 km shallower
 230 than that predicted by the JIVSM (Supplementary Material Figure S4). Such a shallower
 231 bedrock depth in the southern part of the basin is consistent with the results from Yoshimoto
 232 et al. (2009), who used the autocorrelation of S-waves from near-field earthquakes to infer
 233 the bedrock depth using the same stations. Finally, Denolle et al. (2018) showed that the
 234 southern part of the basin is expected to yield strong, complex, and highly variable long-
 235 period ground motions during potential future crustal earthquakes. Therefore, future work

236 is required to refine our understanding of the basin structure in this region and better assess
 237 seismic hazard.

238 The noise ACFs computed in the Kanto Basin are relatively different from that in
 239 other studies (e.g., Saygin et al., 2017; Romero & Schimmel, 2018; Clayton, 2020) as their
 240 frequency content is primarily limited to the 1 to 10 s period range. At higher frequencies
 241 (e.g., 1-3 Hz), noise ACFs do not contain any clear surface-to-bedrock phases (Supplemen-
 242 tary Material Figure S5). A potential explanation is that the attenuation of high-frequency
 243 P-waves in the Kanto Basin is stronger than in other sedimentary basins. This hypothesis is
 244 consistent with the weak and noisy high-frequency (1-3 Hz) earthquake ACF phases (Sup-
 245 plementary Material Figure S5), which are generally well retrieved in other regions (e.g.,
 246 Pham & Tkalčić, 2017). We also note that high-frequency earthquake ACF phases only
 247 appear where the $2p^2$ phases are clearly observed in the 1 to 10 s period range (e.g., in the
 248 region where the four lines intersect).

249 To investigate the cause of the multiples observed at some stations, we simulate the
 250 elastic wave propagation in layered 2-dimensional media at the HYHM and STHM stations
 251 using the SOFI2D package (Supplementary Text and Figure S6 and Table S2, Bohlen et
 252 al., 2016). Both stations are located above relatively flat sedimentary layers to limit the
 253 unwanted contributions from 3-D wave propagation effects (Figures 1a and 2e). We compute
 254 the ACFs of simulated waveforms from two different sources and show that they reproduce
 255 well the noise and earthquake ACFs at the two stations. The ACFs at the STHM station,
 256 where clear multiples can be observed, have a higher frequency content than that at the
 257 HYHM station. The different frequency contents, which are caused by different bedrock
 258 depths, make the multiples appear more or less clearly in the ACFs. Therefore, the difference
 259 of layer thickness and the bedrock depth at the two station locations can explain the presence
 260 (or absence) of P-wave multiples in the noise and earthquake ACFs. However, our 2-
 261 D simulations cannot fully reproduce the noise and earthquake ACFs and future work is
 262 required to better explain the Kanto Basin structure.

263 4 Conclusions

264 We showed that noise and earthquake ACFs computed from the stations of a dense
 265 seismic network can be used to image the bedrock of the complex Kanto Basin. Both
 266 noise and earthquake ACFs contained clear P-wave reflections from which the P-wave two-
 267 way travel time between the surface and the bedrock can be extracted. After migrating
 268 the measured P-wave two-way travel time to depth, we confirmed that the bedrock depth
 269 obtained with both methods agrees well with that from the JIVSM. Our results also showed
 270 that the bedrock in southern part of the basin could be shallower than that predicted by
 271 the JIVSM, which could be critical for seismic hazard assessment. Finally, this study is, to
 272 our best knowledge, the first to use both noise and earthquake ACFs to map the bedrock
 273 shape of an entire basin.

274 In the future, the results from this study could be combined with the promising results
 275 of Chimoto and Yamanaka (2020), who used the autocorrelation of S-waves from nearby
 276 earthquakes to compute the S-wave reflectivity response at several sites in the Kanto basin.
 277 Moreover, a clear next step of this work is to couple the P- and S- reflectivity responses
 278 from ACFs with H/V ratio and/or receiver function analyses to better constrain local 1-D
 279 velocity structures. Such results could finally be combined with a classical ambient noise
 280 surface-wave tomography to refine images of the Kanto Basin and other sedimentary basins
 281 worldwide with dense instrumentation, such as Los Angeles, Seattle, and Mexico City.

282 Acknowledgments

283 We thank the MeSO-net project members for the data and Thanh-Son Pham for the earth-
 284 quake auto-correlation codes and useful discussions. L.V. also thanks Tomotaka Iwata for

285 useful discussions. The MeSO-net data can be downloaded at <https://www.hinet.bosai>
 286 [.go.jp](https://www.hinet.bosai). The Python codes to compute noise ACFs and to reproduce Figures 1-4 will soon
 287 be made available on GitHub. The Python codes to compute noise ACFs will also be in-
 288 cluded in the NoisePy Python package (Jiang & Denolle, 2020). L.V. is supported by the
 289 JSPS Postdoctoral Fellowship for Research in Japan award number P18108.

290 References

- 291 Anderson, J. G., Bodin, P., Brune, J. N., Prince, J., Singh, S. K., Quaas, R., & Onate,
 292 M. (1986). Strong ground motion from the Michoacan, Mexico, earthquake. *Science*,
 293 *233*, 1043–1049. doi: 10.1126/science.233.4768.1043
- 294 Bensen, G. D., Ritzwoller, M. H., Barmin, M. P., Levshin, A. L., Lin, F., Moschetti, M. P.,
 295 ... Yang, Y. (2007). Processing seismic ambient noise data to obtain reliable broad-
 296 band surface wave dispersion measurements. *Geophys. J. Int.*, *169*, 1239–1260. doi:
 297 10.1111/j.1365-246X.2007.03374.x
- 298 Bohlen, T., Nil, D. D., Köhn, D., & Jetschny, S. (2016). *Soft2d seismic modeling with finite*
 299 *differences: 2d – elastic and viscoelastic version* (used under GNU General Public
 300 License, Free Software Foundation). Karlsruhe Institute of Technology.
- 301 Bonnefoy-Claudet, S., Cotton, F., & Bard, P.-Y. (2006). The nature of noise wavefield and
 302 its applications for site effects studies: A literature review. *Earth-Science Reviews*,
 303 *79*, 205–227. doi: 10.1016/j.earscirev.2006.07.004
- 304 Chimoto, K., & Yamanaka, H. (2020, 07). Tuning S-Wave Velocity Structure of Deep Sedi-
 305 mentary Layers in the Shimousa Region of the Kanto Basin, Japan, Using Autocorre-
 306 lation of Strong-Motion Records. *Bull. Seismol. Soc. Am.*. doi: 10.1785/0120200156
- 307 Claerbout, J. (1968). Synthesis of a layered medium from its acoustic transmission response.
 308 *Geophysics*, *33*, 264–269. doi: 10.1190/1.1439927
- 309 Clayton, R. W. (2020, 01). Imaging the Subsurface with Ambient Noise Autocorrelations.
 310 *Seism. Res. Lett.*, *91*, 930-935. doi: 10.1785/0220190272
- 311 Delph, J. R., Levander, A., & Niu, F. (2019). Constraining crustal properties using receiver
 312 functions and the autocorrelation of earthquake-generated body waves. *Journal of*
 313 *Geophysical Research: Solid Earth*, *124*(8), 8981–8997. doi: 10.1029/2019JB017929
- 314 Denolle, M. A., Boué, P., Hirata, N., & Beroza, G. C. (2018). Strong Shaking Predicted in
 315 Tokyo From an Expected M7+ Itoigawa-Shizuoka Earthquake. *J. Geophys. Res. Solid*
 316 *Earth*, *123*, 3968-3992. doi: 10.1029/2017JB015184
- 317 Denolle, M. A., Miyake, H., Nakagawa, S., Hirata, N., & Beroza, G. C. (2014). Long-period
 318 seismic amplification in the Kanto Basin from the ambient seismic field. *Geophys. Res.*
 319 *Lett.*, *41*, 2319–2325. doi: 10.1002/2014GL059425
- 320 Fujiwara, H., Kawai, S., Aoi, S., Morikawa, N., Senna, S., Azuma, H., ... Narita, A.
 321 (2012). Some Improvements of Seismic Hazard Assessment based on the 2011 Tohoku
 322 Earthquake. *Technical Note of the National Research Institute for Earth Science and*
 323 *Disaster Prevention*, *379*.
- 324 Furumura, T., & Hayakawa, T. (2007). Anomalous propagation of long-period ground
 325 motions recorded in Tokyo during the 23 October 2004 Mw 6.6 Niigata-ken Chuetsu,
 326 Japan, earthquake. *Bull. Seismol. Soc. Am.*, *97*, 863–880. doi: 10.1785/0120060166
- 327 Gorbatov, A., Saygin, E., & Kennett, B. L. N. (2013, 12). Crustal properties from seismic
 328 station autocorrelograms. *Geophys. J. Int.*, *192*(2), 861-870. doi: 10.1093/gji/ggs064
- 329 Guéguen, P., Cornou, C., Garambois, S., & Banton, J. (2007). On the Limitation of the
 330 H/V Spectral Ratio Using Seismic Noise as an Exploration Tool: Application to the
 331 Grenoble Valley (France), a Small Apex Ratio Basin. *Pure and Applied Geophysics*,
 332 *164*(1), 115–134. doi: 10.1007/s00024-006-0151-x
- 333 Huang, H.-H., Lin, F.-C., Tsai, V. C., & Koper, K. D. (2015). High-resolution probing of
 334 inner core structure with seismic interferometry. *Geophysical Research Letters*, *42*(24),
 335 10–622. doi: 10.1002/2015GL066390
- 336 Ito, Y., Shiomi, K., Nakajima, J., & Hino, R. (2012). Autocorrelation analysis of ambient
 337 noise in northeastern Japan subduction zone. *Tectonophysics*, *572-573*, 38 - 46. doi:

- 338 <https://doi.org/10.1016/j.tecto.2011.09.019>
- 339 Jiang, C., & Denolle, M. A. (2020). NoisePy: A new high-performance python tool for
340 ambient-noise seismology. *Seismological Research Letters*, *91*(3), 1853–1866. doi:
341 10.1785/0220190364
- 342 Kasahara, K., Sakai, S., Morita, Y., Hirata, N., Tsuruoka, H., Nakagawa, S., . . . Obara, K.
343 (2009, jan). Development of the Metropolitan Seismic Observation network (MeSO-
344 net) for Detection of Mega-thrust beneath Tokyo Metropolitan Area. *Bull. Earthq.*
345 *Res. Inst.*, *84*, 71–88.
- 346 Kennett, B. L., Engdahl, E., & Buland, R. (1995). Constraints on seismic velocities in
347 the earth from traveltimes. *Geophysical Journal International*, *122*(1), 108–124. doi:
348 10.1111/j.1365-246X.1995.tb03540.x
- 349 Koketsu, K., Hatayama, K., Furumura, T., Ikegami, Y., & Akiyama, S. (2005). Damaging
350 long-period ground motions from the 2003 Mw 8.3 Tokachi-oki, Japan earthquake.
351 *Seismol. Res. Lett.*, *76*, 67–73. doi: 10.1785/gssrl.76.1.67
- 352 Koketsu, K., & Kikuchi, M. (2000). Propagation of seismic ground motion in the Kanto
353 basin, Japan. *Science*, *288*, 1237–1239. doi: 10.1126/science.288.5469.1237
- 354 Koketsu, K., Miyake, H., Fujiwara, H., & Hashimoto, T. (2008). Progress towards a
355 Japan integrated velocity structure model and long-period ground motion hazard map.
356 *Proceedings of the 14th World Conference on Earthquake Engineering*, S10–038.
- 357 Koketsu, K., Miyake, H., & Suzuki, H. (2012). Progress towards a Japan integrated velocity
358 structure model and long-period ground motion hazard map. *Proceedings of the 15th*
359 *World Conference on Earthquake Engineering*, 1773.
- 360 Kudo, K. (1978). The contribution of Love waves to strong ground motions. *Proceedings of*
361 *the 2nd International Conference on Microzonation*, *2*, 765–776.
- 362 Kudo, K. (1980). A study on the contribution of surface wave to strong ground motions.
363 *Proceedings of the 7th World Conference on Earthquake Engineering*, 499–506.
- 364 Langston, C. A. (1979). Structure under Mount Rainier, Washington, inferred from teleseis-
365 mic body waves. *Journal of Geophysical Research: Solid Earth*, *84*(B9), 4749–4762.
366 doi: 10.1029/JB084iB09p04749
- 367 Leahy, G. M., Saltzer, R. L., & Schmedes, J. (2012). Imaging the shallow crust with
368 teleseismic receiver functions. *Geophysical Journal International*, *191*, 627–636. doi:
369 10.1111/j.1365-246X.2012.05615.x
- 370 Lin, F.-C., & Tsai, V. C. (2013). Seismic interferometry with antipodal station pairs.
371 *Geophysical Research Letters*, *40*(17), 4609–4613. doi: 10.1002/grl.50907
- 372 Liu, G., Persaud, P., & Clayton, R. W. (2018, 08). Structure of the Northern Los Angeles
373 Basins Revealed in Teleseismic Receiver Functions from Short-Term Nodal Seismic
374 Arrays. *Seismological Research Letters*, *89*(5), 1680–1689. doi: 10.1785/0220180071
- 375 Mamula, L., Kudo, K., & Shima, E. (1984). Distribution of ground-motion amplification
376 factors as a function of period (3–15 s), in Japan. *Bull. Earthq. Res. Inst.*, *59*, 467–500.
- 377 Morrice, D. J., Kenyon, A. S., & Beckett, C. J. (2001). Optimizing operations in 3-d land
378 seismic surveys. *Geophysics*, *66*(6), 1818–1826. doi: 10.1190/1.1487124
- 379 Nakamura, Y. (1989). A method for dynamic characteristics estimation of subsurface using
380 microtremor on the ground surface. *Quarterly Report of Railway Tech. Res. Inst.*, *30*,
381 25–30.
- 382 Oren, C., & Nowack, R. L. (2016). Seismic body-wave interferometry using noise auto-
383 correlations for crustal structure. *Geophysical Journal International*, *208*, 321–332.
384 doi: <https://doi.org/10.1093/gji/ggw394>
- 385 Pham, T.-S., & Tkalčić, H. (2017). On the feasibility and use of teleseismic p wave coda
386 autocorrelation for mapping shallow seismic discontinuities. *J. Geophys. Res. Solid*
387 *Earth*, *122*, 3776–3791. doi: 10.1002/2017JB013975
- 388 Pham, T.-S., & Tkalčić, H. (2018). Antarctic ice properties revealed from teleseismic p
389 wave coda autocorrelation. *Journal of Geophysical Research: Solid Earth*, *123*(9),
390 7896–7912. doi: 10.1029/2018JB016115
- 391 Romero, P., & Schimmel, M. (2018). Mapping the basement of the ebro basin in spain with
392 seismic ambient noise autocorrelations. *J. Geophys. Res. Solid Earth*, *123*, 5052–5067.

- doi: 10.1029/2018JB015498
- 393 Sakai, S., & Hirata, N. (2009, jan). Distribution of the Metropolitan Seismic Observation
 394 network. *Bull. Earthq. Res. Inst.*, *84*, 57–69.
- 395 Saygin, E., Cummins, P. R., & Lumley, D. (2017). Retrieval of the P wave reflectivity
 396 response from autocorrelation of seismic noise: Jakarta Basin, Indonesia. *Geophys.*
 397 *Res. Lett.*, *44*, 792–799. doi: 10.1002/2016GL071363
- 398 Schimmel, M., & Paulssen, H. (1997, 08). Noise reduction and detection of weak, coherent
 399 signals through phase-weighted stacks. *Geophys. J. Int.*, *130*, 497–505. doi: 10.1111/
 400 j.1365-246X.1997.tb05664.x
- 401 Takemura, S., Akatsu, M., Masuda, K., Kajikawa, K., & Yoshimoto, K. (2015). Long-period
 402 ground motions in a laterally inhomogeneous large sedimentary basin: observations
 403 and model simulations of long-period surface waves in the northern Kanto Basin,
 404 Japan. *Earth Planets Space*, *67*, 33. doi: 10.1186/s40623-015-0201-7
- 405 Tibuleac, I. M., & von Seggern, D. (2012, 04). Crust-mantle boundary reflectors in Nevada
 406 from ambient seismic noise autocorrelations. *Geophys. J. Int.*, *189*(1), 493–500. doi:
 407 10.1111/j.1365-246X.2011.05336.x
- 408 Tkalčić, H., Phạm, T.-S., & Wang, S. (2020). The earth’s coda correlation wavefield:
 409 Rise of the new paradigm and recent advances. *Earth-Science Reviews*, 103285. doi:
 410 10.1016/j.earscirev.2020.103285
- 411 Tork Qashqai, M., Saygin, E., & Kennett, B. (2019). Crustal imaging with Bayesian
 412 inversion of teleseismic P wave coda autocorrelation. *Journal of Geophysical Research:*
 413 *Solid Earth*, *124*(6), 5888–5906.
- 414 Viens, L., Koketsu, K., Miyake, H., Sakai, S., & Nakagawa, S. (2016). Basin-scale Green’s
 415 functions from the ambient seismic field recorded by MeSO-net stations. *J. Geophys.*
 416 *Res. Solid Earth*, *121*, 2507–2520. doi: 10.1002/2016JB012796
- 417 Wang, T., Song, X., & Xia, H. H. (2015). Equatorial anisotropy in the inner part of
 418 earth’s inner core from autocorrelation of earthquake coda. *Nature Geoscience*, *8*(3),
 419 224–227.
- 420 Wapenaar, K. (2003). Synthesis of an inhomogeneous medium from its acoustic transmission
 421 response. *Geophysics*, *68*, 1756–1759. doi: <https://doi.org/10.1190/1.1620649>
- 422 Yamada, N., & Yamanaka, H. (2012). 3d s-wave velocity model of kanto basin for long-period
 423 ground motion simulation with special focus on treatment of shallow near-surface part.
 424 *Butsuri Tansa (Geophysical Exploration)*, *65*(3), 139–150. doi: 10.3124/segj.65.139
- 425 Yoshimoto, K., Sakurai, K., Nakahara, H., Kinoshita, S., & Sato, H. (2009). Seismic
 426 basement structure beneath the Kanto plain, Japan inferred from the seismic inter-
 427 ferometry for strong motion records. In *Symposium on “seismic wave scattering and*
 428 *noise correlation”*. Tohoku University.
- 429 Yoshimoto, K., & Takemura, S. (2014). Surface wave excitation at the northern edge
 430 of the Kanto Basin, Japan. *Earth, Planets and Space*, *66*(1), 16. doi: 10.1186/
 431 1880-5981-66-16
- 432

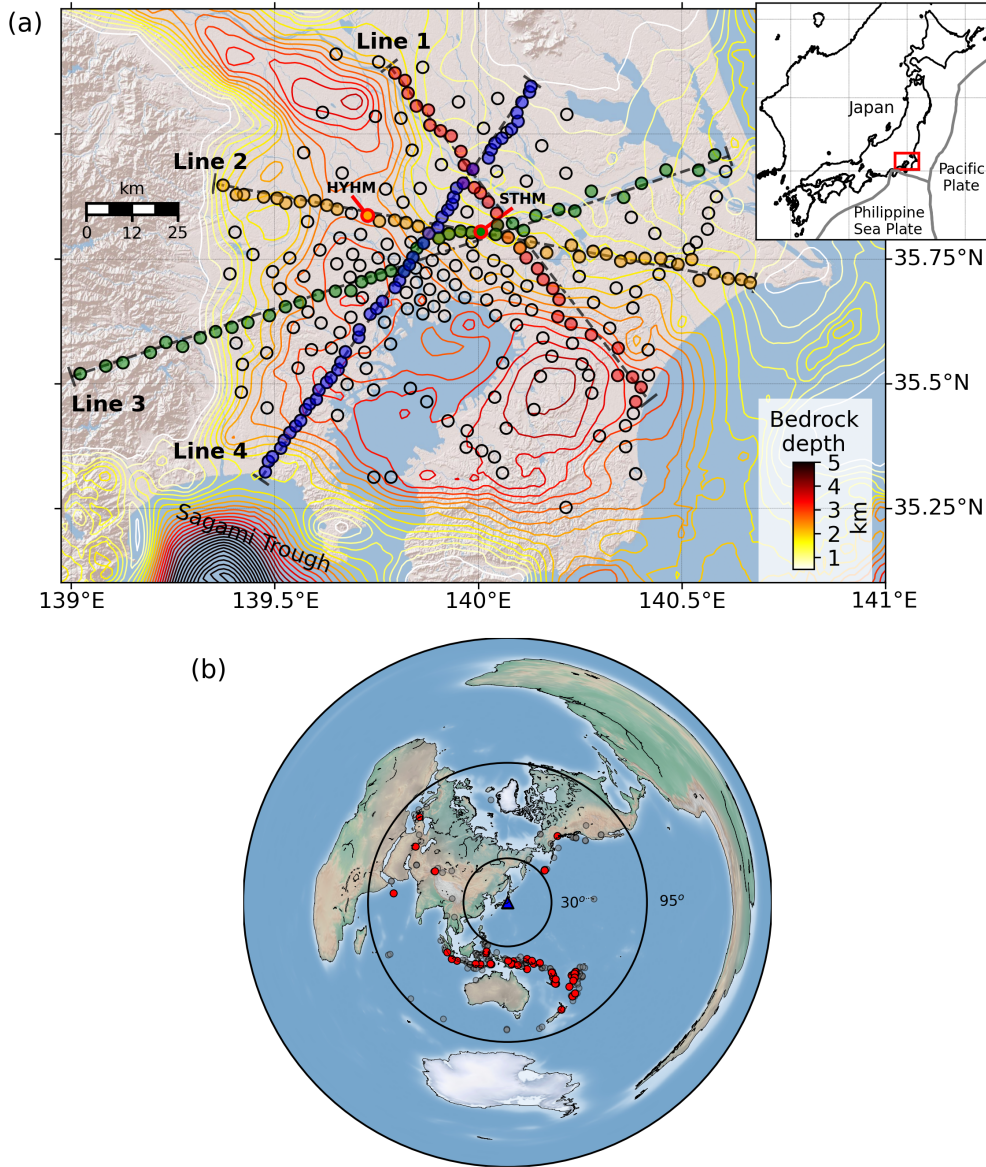


Figure 1. (a) Topographic map of Kanto region including the 287 MeSO-net stations (circles) and 250-m-spaced bedrock iso-depth contours ($V_P = 5.5$ km/s) from the JIVSM (colored lines, Koketsu et al., 2008, 2012). The stations aligned along Line 1 (red), Line 2 (orange), Line 3 (green), and Line 4 (purple) are also highlighted. The HYHM and STHM station locations are shown by the red edge circles. The four JIVSM profiles in Figures 2 and 3 are taken along the back dashed lines. The inset map shows the Japanese Islands (black lines), the region of interest (red rectangle), and the plate boundaries (gray lines). (b) Azimuthal equidistant projection map centered on the Kanto Basin including the 244 $M_w \geq 6$ earthquakes which occurred within 30 and 95 degrees from the Kanto Basin between May 2017 and 2020 (gray circles). The locations of the 50 selected earthquakes are shown by red circles.

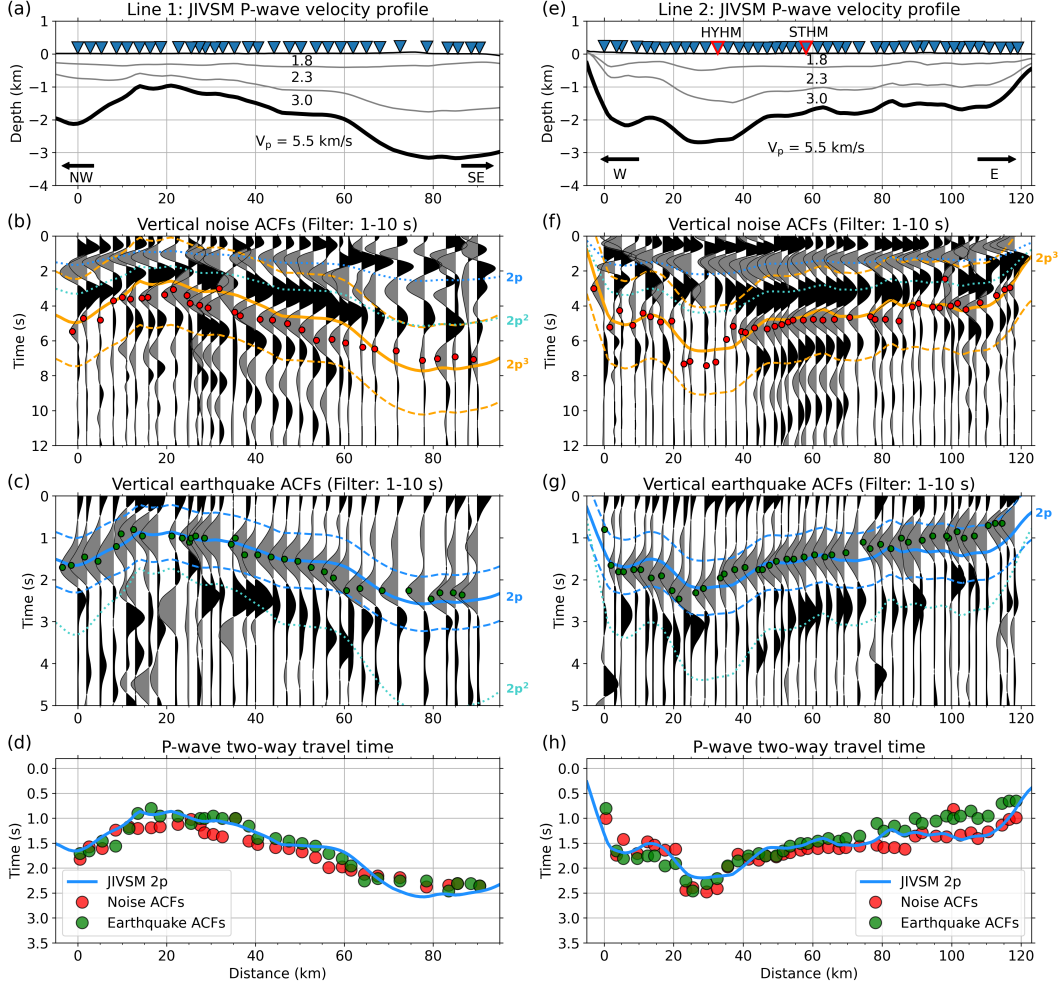


Figure 2. (a) JIVSM velocity profile along Line 1 including the P-wave velocity of each layer. The basin bedrock is highlighted by the thick black line and the orientation of the profile is also indicated (e.g., NW: north-west; SE: south-east). (b) Noise ACFs along Line 1 bandpass filtered between 1 and 10 s. The dotted blue and light blue lines highlight the theoretical $2p$ and $2p^2$ arrival times between the surface and the bedrock, respectively. The thick orange line shows the theoretical $2p^3$ arrival time and the dashed orange lines are the $2p^3$ arrivals ± 2.5 s. The red filled circles are the selected negative peaks used in this study. (c) Earthquake ACFs bandpass filtered between 1 and 10 s. The thick blue and dotted light blue lines represent the theoretical $2p$ and $2p^2$ arrival times. The dashed blue lines are the blue line ± 0.65 s. The green dots are the negative peaks selected in this study. Note that the vertical time axes in (b) and (c) are different. (d) Theoretical P-wave two-way travel time ($2p$, blue line) and the values obtained from noise ACFs divided by three (red circles) and that from earthquake ACFs (green circles). (e-h) Same as (a-d) for Line 2. The HYHM and STHM station locations along Line 2 are also indicated.

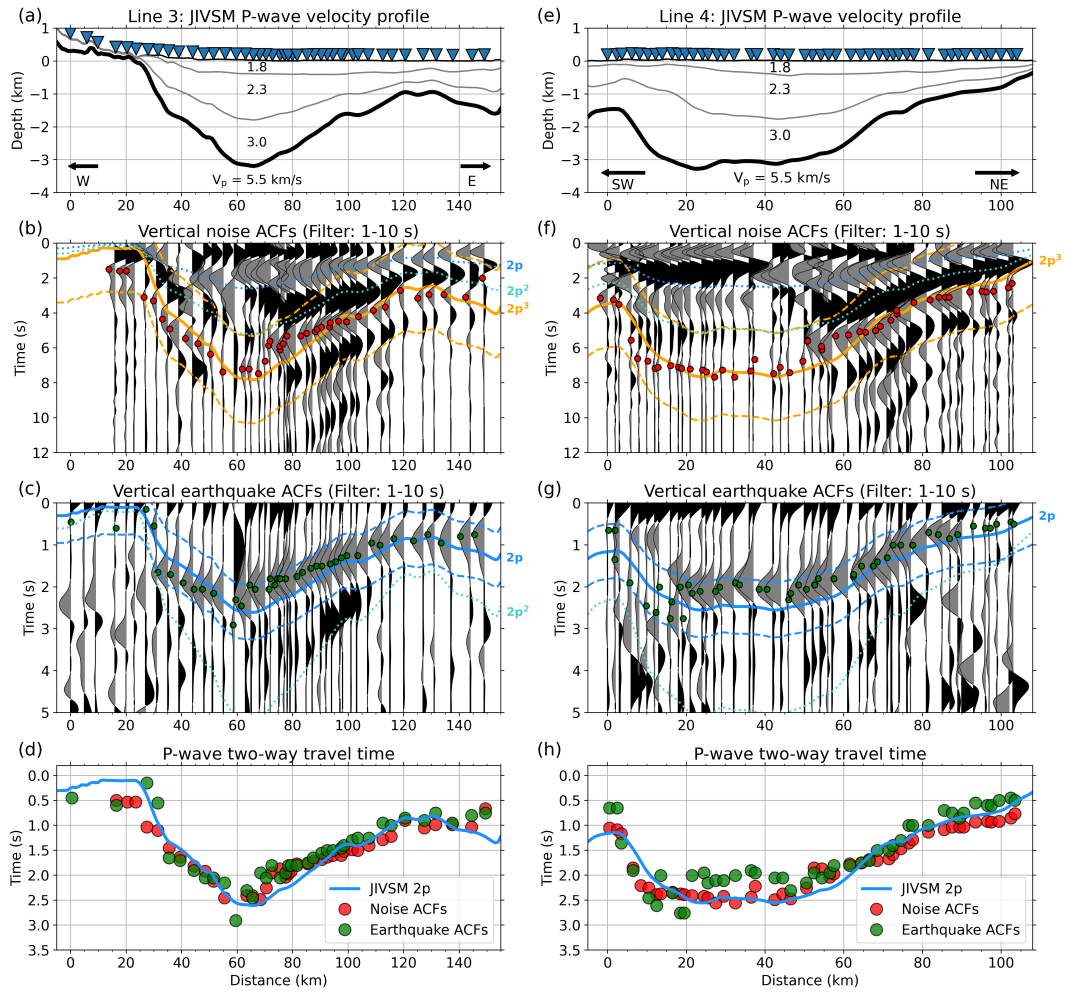


Figure 3. Same as Figure 2 for the stations along Line 3 (a-d) and Line 4 (e-h).

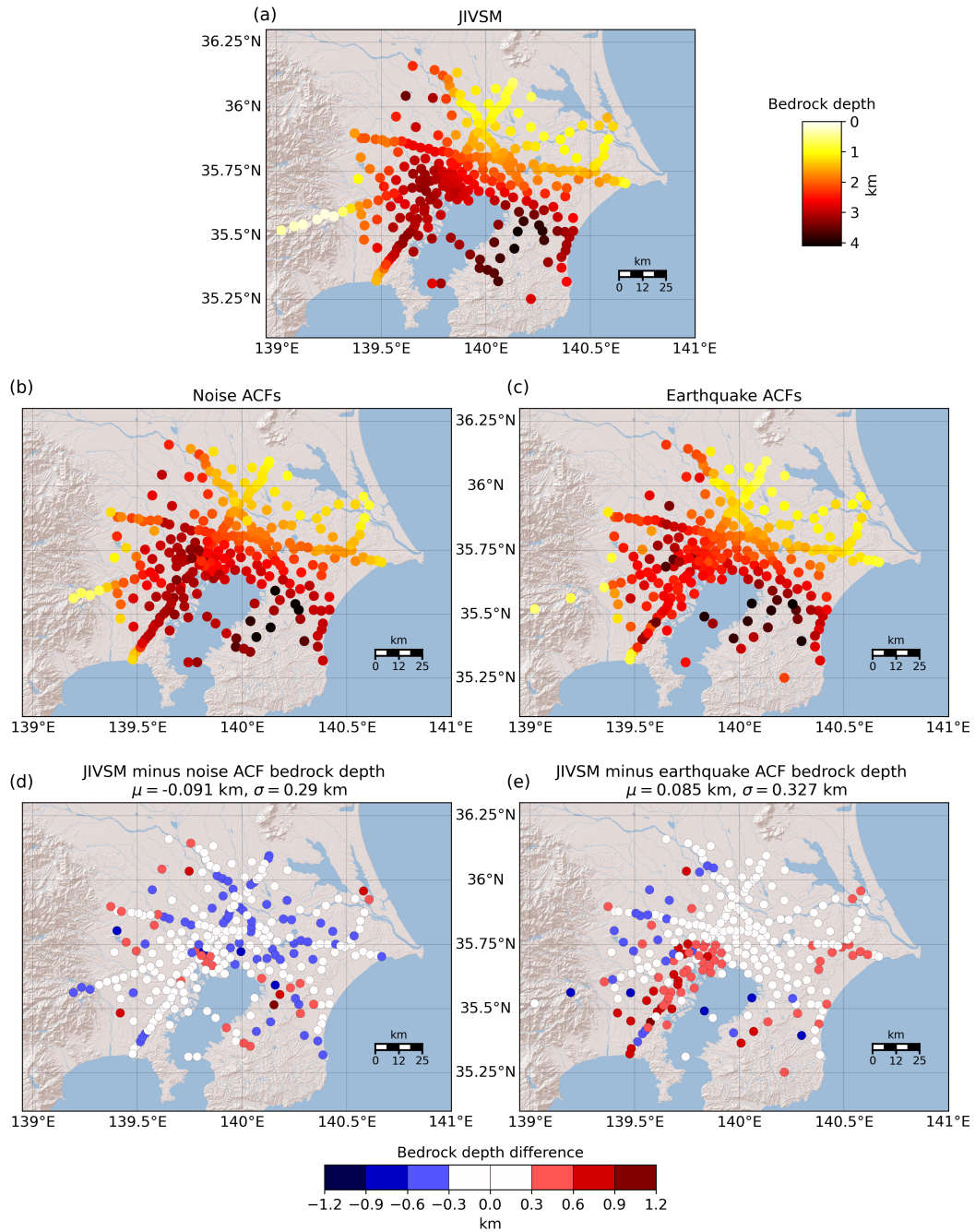


Figure 4. Basin bedrock depth beneath each station from (a) the JIVSM, (b) noise ACFs, and (c) earthquake ACFs. The noise and earthquake bedrock depths are obtained by migrating the P-wave two-way travel times to depth with a constant P-wave velocity of 2.53 km/s. Residuals between the JIVSM bedrock depth minus that from (d) noise ACFs and (e) earthquake ACFs. Blue and red filled circles indicate that the JIVSM bedrock depths are shallower and deeper than that from the ACFs, respectively. The mean of the residuals over all the stations (μ) and the one standard deviation to the mean (σ) are also indicated.